

One-Step Site-Specific Activation Approach for Preparation of Hierarchical Porous Carbon Materials with High Electrochemical Performance

Zongze Lv,[†] Xiaoli Li,^{*,‡} Xiujuan Chen,[§] Xiang Li,[†] Meng Wu,[‡] and Zhiguo Li^{*,†}

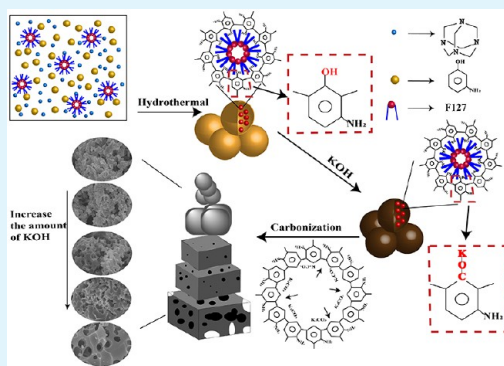
[†]Key Laboratory of Bio-based Material Science and Technology, Ministry of Education, College of Materials Science and Engineering, and [‡]College of Chemistry, Chemical Engineering and Resource Utilization, Northeast Forestry University, Harbin, Heilongjiang 150040, China

[§]Mechanical & Aerospace Engineering Department, West Virginia University, Morgantown, West Virginia 26506, United States

Supporting Information

ABSTRACT: Precise control of carbonization and activation for fabricating novel carbon materials and improving practical performance have continued to be a big challenge. Inspired by the aggregation of abundant inorganic elements on a special part in biomass for self-activation, we developed a novel site-specific activation strategy to prepare porous carbon materials with controllable morphology and microstructure based upon regulating the activator molecule distribution for aggregation of activators on specific sites in a carbonaceous precursor. The fabrication of porous carbons was carried out not only in one step of direct calcination but with much reduced use of activators, demonstrating comparative or even preferable structure and performance characteristics of porous carbon compared with that of the conventional activated method. Porous carbons featured with a 3D flake interconnection network were obtained by site-specific activation with hierarchical porosity and unique micropore size distribution. The obtained porous carbon materials displayed excellent electrochemical performance with high specific capacitance (375 F g^{-1} at 0.1 A g^{-1}) and excellent capacitance retention (276 F g^{-1} at 20 A g^{-1}) used as electrode materials. Meanwhile, the symmetric supercapacitors assembled by the porous carbon could yield specific energy density up to 7.81 Wh kg^{-1} with excellent power density (9600 W kg^{-1}) and outstanding cycling stability (99.8% capacitance retention after 10 000 charge/discharge cycles at 2 A g^{-1}) in $1 \text{ M H}_2\text{SO}_4$ electrolytes.

KEYWORDS: hierarchical porous carbon, one-step site-specific activation, morphological transformation, carbon electrode materials, supercapacitors



1. INTRODUCTION

Porous carbon materials have been extensively explored and applied as one of the most important carbons due to their wide availability and superior physicochemical properties.^{1–3} The featured structure of porosity, specific surface area, and pore volume, and the practical performance related to energy storage, catalysis, and macromolecular adsorption of the porous carbons could be significantly improved by the conduction of the activation procedure, especially chemical activation which has been extensively applied for carbon materials. In the conventional chemical activation approach, activated porous carbons are customarily prepared by a two-step process composed of carbonization of carbon-rich precursors at high temperature and subsequent activation of the carbonized products (obtained in the previous carbonization process at high temperature, abbreviated to precarbonized materials (PCMs) for simplification) blending with activator to increase the specific surface area and pore volume in inert atmosphere.^{4–6} Intrinsically, the carbonization at high

temperature dramatically reduced the wettability of the PCMs, so the chemical activators remained mainly on the surface of the PCMs after being mixed with activators due to the poor compatibility or solubility between the PCMs and activators such as KOH. The phenomenon that the poor wettability of the PCMs would result in that the activation could only be occurred on the surface of the PCMs, and a large quantity of chemical activators consumption is required to achieve the ideal activation for porous carbons. Meanwhile, the influence of conventional activation was mainly executed on the micropore development through etching the surface carbons of PCMs by activator, but less effect was observed on the morphological and structural optimization that is always required for porous carbons with specific morphology and texture to achieve perfect performance at the greatest extent in

Received: September 5, 2019

Accepted: November 27, 2019

Published: November 27, 2019

many applications. Therefore, it is essential to explore novel strategies for improving and optimizing the activation of porous carbons through eliminating the multiple heat treatments and low activation efficiency of activators which was brought about by the conventional activation.

Enhancement of the wettability or even solubility of PCMs with activators is an obvious prerequisite to improve the activation effect for synthesis of porous carbons. Recently, a one-step activation approach has been developed to prepare activated porous carbon, which omitted the carbonization step at high temperature and directly mixed carbonaceous precursors with chemical activators for activated calcination based on the good wettability of carbonaceous precursors with activators. Compared with the conventional two-step activation, the excellent wettability of carbonaceous precursors could make the activators enter the interior of the precursors, instead of just staying on the surface, to achieve overall activation in a more effective way to develop the porous structure of carbon materials. At present, the effective execution of the one-step activation mainly relies on the carbonaceous precursor property which is mostly derived from synthetic polymers⁷ and biomass precursors displaying excellent hydrophilicity or even solubility with chemical activators.^{8–11} For example, agar could be soluble with hot KOH solution, leading to homogeneous deoxygenation and further molecular level distribution of KOH in agar for one-step calcination to prepare activated carbon with superior specific surface area and pore volume.⁹ Moreover, carbon morphology and texture could be dramatically altered when the one-step chemical activation procedure was carried out, because inevitable massive gases from the whole internal precursors would extrude the carbon structure based upon the excellent compatibility of carbonaceous precursors with activators.¹⁰ The possible transformation on carbon morphology and texture could be made by fabricating novel carbon materials including 3D highly hierarchical porous carbon or even 2D carbon nanosheets with unique textural characteristics and advanced performance, which is clearly distinguished from that produced from the conventional two-step activation process and showed great potential in supercapacitors and gas adsorption with high performance to develop 3D HPCs (containing micro-, meso-, and macropores).¹¹ Although considerable attention has been paid to obtain novel porous carbons through the one-step activation method, the lack of adjustment and regulation over activated sites in the carbonaceous precursors during the calcination process due to random distribution of activators in the carbonaceous precursor offers poor control of pore formation and pore size distribution for further advanced performance of porous carbons. Thus, it still remains a big challenge to precisely control activation through a cost-effective process by simply modifying the conventional activation procedure for fabrication of novel porous carbon materials with greatly advanced performance.

Control over activated sites through restricting the distribution of the activator molecular on the carbonaceous precursor apparently plays a key role in pore formation and development of the porous carbons. Biomass precursors would provide a feasible reference for tunable sites for one-step activation derived from aggregation of inorganic elements in specific parts. Apparently, for a tree, the enrichment of inorganic elements was varied from different parts of the tree, and many more metal ions including K, Ca, Mg, and Na are

confined into leaves for photosynthesis, leading to higher content of metal ions in leaves than that of other parts. Dead leaves with high metal ion content could be directly calcinated as carbonaceous precursors, exhibiting well-defined pores and large surface area which could be fully attributed to the self-activation effect of abundant metal elements aggregated in leaves. The porous carbons derived from leaves displayed outstanding electrochemical performance as electrodes for supercapacitors compared with that from other parts of the tree, demonstrating the significant effect of metal ion aggregation in specific parts on the property of the porous carbons.¹² Meanwhile, inorganic elements like sodium ions could be introduced into the lignin derivatives at the molecular level for self-activation of biomass precursors, implying that the distribution of metal ions in carbonaceous precursors could be regulated by chemical modification.¹³ The above discussion shows that self-activation originated from enrichment of metal ions in biomass precursors is a carbon-consuming process. Pore-forming and pore-expanding in carbons are realized by the reaction of active metal ions with carbon atoms to form carbonates at high temperature,¹³ indicating that the distribution of metal ions in carbonaceous precursors would play a dominant role to the porosity and texture of the porous carbons. Furthermore, the adjustment of porous distribution in carbons could be induced by metal ions distribution on the carbonaceous precursors in a designed way through chemical reaction, suggesting the potential of remarkable transformation of the carbon morphology and structure.

Inspired by the phenomenon of biomass activation, a novel site-specific activation strategy for preparing porous carbons is proposed based on the aggregation of reactive metal ions in carbonaceous precursors by a predesigned method. It can be deduced that active metal ions could be fixed at the specific sites in the carbonaceous precursor by reacting with functional groups. Thus, the aggregation and adjustment of the activators could be achieved in a designed way through regulating the distribution of functional groups in the precursor. For the proof-of-concept study, phenolic resin assembled with Pluronic F127 is selected as synthetic precursor to explore the site-specific activation for fabricating porous carbons. The reaction of activator, KOH, with phenolic hydroxyl groups will form $-C-O-K$ functional groups,^{14,15} acting as the specific point of subsequent activation though decomposition at high temperature. It has been proven that the presence of Pluronic F127 would cause phenolic hydroxyl groups to gather around Pluronic F127 during the hydrothermal process, changing the distribution of phenolic hydroxyl groups in the phenolic resin.¹⁶ The K ions are immobilized at the phenolic hydroxyl groups in the form of $-C-O-K$, indicating that the distribution of specific sites, $-C-O-K$, could be adjusted through regulating phenolic hydroxyl groups in carbonaceous precursors. Attributed to the improved control over the activated sites, the porous structure is significantly altered, resulting in the morphological and textural transformation of the porous carbons. Finally, porous carbons with highly hierarchical porosity are controllably produced, which is favorable for rapid ion contact diffusion and energy storage. Using electrode materials as supercapacitors, the produced porous carbons displayed excellent electrochemical performance and outstanding cyclic stability in aqueous electrolyte.

2. EXPERIMENTAL SECTION

2.1. Preparation of Site-Specific Activated Porous Carbon Materials (S-PCM). In a typical experimental procedure, 0.55 g *m*-aminophenol, 0.35 g hexamethylenetetramine (HMT), 1.00 g Pluronic F127, and 0.20 g 1,3,5-trimethylbenzene (TMB) were dispersed in a 17.50 g deionized water mixture with 0.50 g of sulfuric acid solution (1 mol L⁻¹) and magnetically stirred for 2 h at room temperature. Then the obtained homogeneous solution was transferred into a 50 mL Teflon-lined stainless steel autoclave, and heated at 100 °C for 24 h. After cooling down to room temperature spontaneously, the resulting precipitate and APF (*m*-aminophenol formaldehyde)-F127 polymer were filtered, washed with ethanol followed by deionized water several times, and dried at 80 °C to obtain the product. Subsequently, 1.8 g of the as-prepared polymer and a given amount of KOH were mixed in 10 mL deionized water and then dried at 80 °C to obtain the product. In this study, the added amount of KOH was varied to be 0.1, 0.2, 0.3, 0.6, and 0.9 g, which were calculated as 3:1, 3:2, 1:1, 1:2, and 1:3 in molar ratio of phenolic hydroxyl group:KOH, respectively. The blends then were heated to 650 °C with a ramping rate of 1 °C min⁻¹ and maintained for 2 h in a tubular furnace under a high purity argon atmosphere. After cooling, the obtained products were thoroughly washed with 0.2 M HCl solution and deionized water to ensure no residual alkali and inorganic salts. The samples were finally collected after drying at 80 °C for 12 h. The obtained porous carbon materials were labeled as S-PCM 3:1, S-PCM3:2, S-PCM1:1, S-PCM1:2, and S-PCM1:3.

2.2. Preparation of Disordered Activated Porous Carbon Materials (D-PCM). Hydrothermal products without Pluronic F127 were produced in the same way and labeled as D-PCM to compare with S-PCM. Subsequently, D-PCM and KOH were blended in proportion to phenolic hydroxyl group (hydroxyl group:potassium hydroxide in molar ratio was 1:0 (0.8 g:0 g) 1:1 (0.8 g:0.3 g), and 3:2 (0.8 g:0.6 g)) and stirred with deionized water (10 g). The blends were carbonized under the same conditions and labeled as D-PCM1:0, D-PCM1:1, and D-PCM1:2 to compare with S-PCM1:1 and S-PCM1:2.

2.3. Preparation of Ordered Mesoporous Carbons (OMC) and Conventional Activated Porous Carbon Materials (C-PCM). In order to compare with conventional preparation methods, the brick-red precipitate, APF (*m*-aminophenol formaldehyde)-F127 polymer was carbonized by heating at 650 °C for 2 h in a tubular furnace under a high purity argon atmosphere with a ramping rate of 1 °C min⁻¹, and the obtained products were labeled as OMC. The OMC were further chemically activated with KOH, as reported in detail elsewhere.¹⁷ In these experiments, 0.4 g of the mesoporous carbon microspheres were immersed in KOH solution (1.6 g KOH in 4 g of H₂O), followed by a water evaporation step at 100 °C under vacuum. Afterward, the impregnated samples were heated to the desired temperature of 650 °C with a heating rate of 10 °C min⁻¹ and maintained for 1 h. After cooling in a flowing high purity argon atmosphere, the obtained products were thoroughly washed with 0.2 M HCl solution and deionized water until the filtrate became neutral, and finally dried at 80 °C for 12 h. The products obtained by conventional two-step activation procedure were labeled as C-PCM.

2.4. Materials Characterizations. For characterizing the morphology of the samples, a field-emission Sirion scanning electron microscope (SEM) and an H-7650 transmission electron microscope (TEM) at operating voltage of 100 kV were used. The crystalline phase of the as-prepared materials was analyzed by wide-angle X-ray diffraction measurements (XRD), which was taken on an X'Pert PRO MPD X-ray diffractometer using Ni-filtered Cu K α radiation source. A Fourier-transform infrared (FTIR) spectrometer (Shimadzu Spectrum One FTIR) was used to analyze the change of functional groups of the precursor. The X-ray photoelectron spectroscopy (XPS) characterizations were carried out on an ESCALAB250Xi spectrometer with Al K α radiation ($h\nu = 1486.6$ eV) to reveal the surface chemical elements of the samples. The porous texture of the samples was analyzed by nitrogen adsorption-desorption isotherms on a 3H-2000PM1 analyzer (Beishide, China) at 77 K.

2.5. Electrochemical Measurements. The electrochemical performances were assessed with both three-electrode cell and two-electrode symmetric supercapacitor. The porous carbon material was first mixed with polytetrafluoroethylene (PTFE) binder and acetylene black at a weight ratio of 80:10:10 to obtain pastes, then spread on a 1 \times 1 cm² stainless steel mesh and a circular stainless-steel mesh with diameter of 1.4 cm. The paste was compressed at 10 MPa for 2 min, followed by drying for 10 h at 100 °C in a vacuum oven. The mass loading of the active materials in each electrode was ~ 2.3 mg cm⁻². The traditional three-electrode systems were accomplished in 1 M H₂SO₄ aqueous solution. The coated nickel foam (1 \times 1 cm²) served as the working electrode, a platinum foil as the counter electrode, and a Hg/Hg₂SO₄ electrode as the reference electrode. CV tests were executed at various scanning rates ranging from 10 to 200 mV s⁻¹. GCD tests were performed at a range of current density from 0.5 to 20 A g⁻¹. EIS measurements were recorded from 10⁵ kHz to 10⁻² Hz at the open-circuit potential with an alternate current amplitude of 5 mV. In a typical two-electrode system, the symmetric supercapacitor device was assembled with a 2025-type coin cell. The two S-PCMs based electrodes with the same size and sample weight were first prewetted with 1 M H₂SO₄ electrolyte, separated by a thin polypropylene film, and then packed into one two-electrode cell (Figure S1). The potential window for the supercapacitors using 1 M H₂SO₄ was set at -0.7 to 0.3 V. The test of long-term cycling stability was carried out on a supercapacitor test system (Neware, Guangdong, China).

According to the charge/discharge curves, the specific capacitance of the C-PCMs could be calculated based on the following equation:

$$C_m = \frac{I_d \times \Delta t}{\Delta V \times m} \quad (1)$$

$$C_{sp} = 4C_m \quad (2)$$

where C_m (F g⁻¹) is the specific capacitance, I_d (mA) is the discharge current, Δt (s) is the discharge time, and ΔV (V) is the discharge voltage range which is exclusive of the IR drop. In a three-electrode system, m (mg) represents the mass loading of active material for a single electrode, and in a two-electrode cell, m (mg) is the total mass of active materials for two electrodes. C_{sp} (F g⁻¹) is the specific capacitance of a single electrode in in two-electrode cell.

The energy density E (W h kg⁻¹) and power density P (W kg⁻¹) were calculated based on GCD tests by the following equations:

$$E = \frac{0.5C_m \times \Delta V^2}{3.6} \quad (3)$$

$$P = \frac{E}{\Delta t} \times 3600 \quad (4)$$

where C_m (F g⁻¹) is the specific capacitance based on the total mass of active materials in both electrodes. ΔV (V) is the discharge voltage after exclusion of the IR drop, Δt (s) is the discharge time.

The Coulombic efficiency was calculated based on the strength of the following equations:

$$\eta = \frac{t_d}{t_c} \times 100\% \quad (5)$$

where t_d (s) is the discharge time and t_c (s) is the charge time.

3. RESULTS AND DISCUSSION

3.1. Materials Characterization. The morphology of the prepared samples was investigated by SEM and TEM as shown in Figure 1 and Figures S2–8. It can be seen from the SEM images that the OMC was composed of coral-like spherical particles with multiple interconnected patches, and ordered mesopores were formed in the spherical particles as presented in the TEM image, which came from the self-assembly of phenolic resin induced by Pluronic F127 as the soft template. By conventional two-step activation, the activated C-PCM

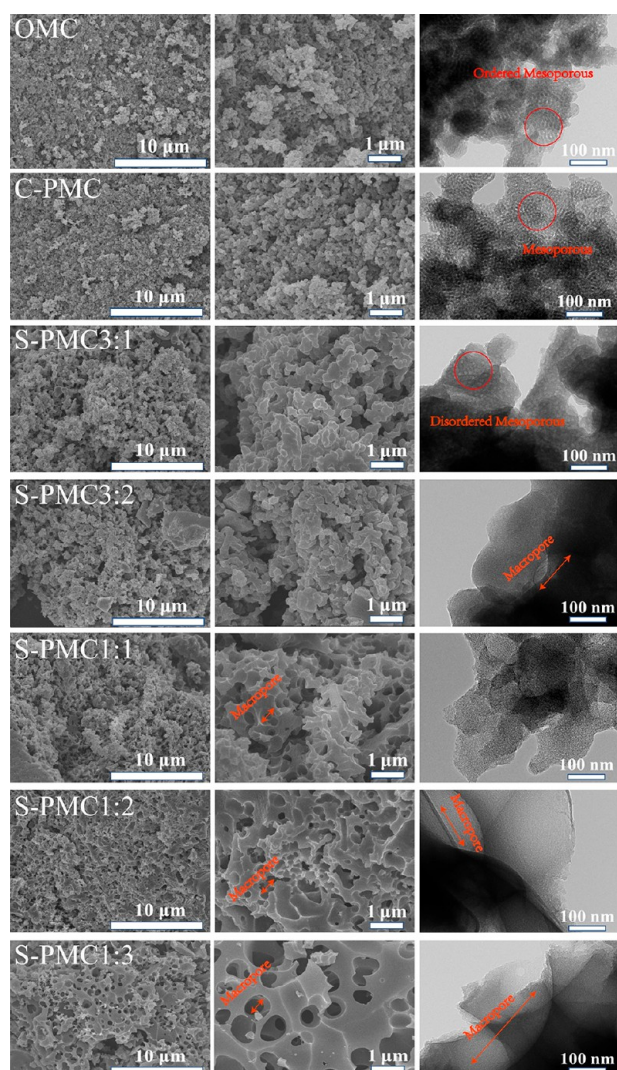


Figure 1. Typical SEM (10 μm scale and 1 μm scale) and TEM (100 nm scale) images of the prepared samples.

from OMC with KOH in a mass ratio of 1:4 maintained the original morphology of coral-like spherical particles. It should be noted that the orientation of mesopores in the particle was partially disturbed, demonstrating that the conduction of conventional activation on pore development was executed through surface corrosion without texture alternation, whereas when the site-specific activation strategy was adopted, remarkable variation on morphology and texture of the products occurred with a slight KOH dosage. With the molar ratio of phenolic hydroxyl groups to KOH at 3:1, although the coral-like morphology remained the same as that of OMC, the carbon bulk of S-PMC3:1 was obviously expanded, and ordered mesopores in carbon were replaced by larger disordered mesopores. The textural variation on porous orientation with enlarged size could be ascribed to the site-specific activation, further expanding the mesopores. It is noteworthy that the KOH dosage in site-specific activation was proportional to the phenolic hydroxyl groups in molar content, which was far below the mass ratio of carbons to activators at 1:4 that is usually applied in the conventional activation. As in the example of S-PMC3:1, the molar ratio of phenolic hydroxyl groups to KOH at 3:1; in term of mass ratio, it was only 18:1 with carbonaceous precursor to KOH, several tenths of KOH

dosage compared with that applied in a conventional activation route for C-PCM. Thus, the carbons produced by the site-specific activation exhibited an obvious textural change at a slight amount of KOH, which was quite different from that by conventional activation. When the molar ratio of phenolic hydroxyl group to KOH was increased to 3:2, the internal pore of S-PMC3:2 was further enlarged and transformed from a disordered mesopore to a large macropore. The inner wall between mesopores might collapse with the increase of KOH dosage, resulting in the formation of macropores. Once the ratio reached 1:1, where all the phenolic hydroxyl groups in the carbonaceous precursor were theoretically reacted with KOH, the morphology was dramatically altered to form a 3D carbon network structure with macrovoids of several micrometers and a wall of a few hundred nanometers. The variation in carbon morphology resulted from the transformation of the inner pore into the outer wall of carbons, originating from collapse of the outer wall during activation at high temperature. Since the reaction of KOH with a phenolic hydroxyl group was reversible, all the phenolic hydroxyl groups in the carbonaceous precursor were completely reacted with KOH when the ratio was higher than 1:1 during site-specific activation, leading to the formation of 3D interconnected carbon flakes. The samples prepared in a ratio of 1:2 were composed of thin carbon flakes connected with each other, which featured randomly disclosed micropores as presented in S-PCM1:2. By further increasing the ratio to 1:3, the sample retained the morphology of the 3D interconnected flake network with many conspicuous macropores with walls of dozens of nanometers, indicating that the morphology and structure were no longer altered in a dramatic way with the variation of KOH dosage. It can be concluded that the morphology and texture of the as-prepared porous carbon could be significantly altered with small amount of KOH dosage by site-specific activation in one-step, which was quite different from the conventional two-step activation method. Moreover, the morphology transformation was controllable by adjusting activator amount, demonstrating the improved controllability over the activation of porous carbons.

To further explore the pore properties of the as-prepared samples, the nitrogen adsorption/desorption isothermal analysis was carried out at 77 K (Figure 2 and Figure S9). All the S-PCMs samples exhibited a typical type I sorption isotherm, implying the existence of micropores in S-PCMs structure.^{8,17} Meanwhile, a weak retention closed loop in the relative pressure range from 0.1 to 0.9 could be observed in each isotherm of S-PCMs, indicating that the S-PCMs retained a certain amount of mesopore.¹⁸ It could be further verified by the pore size distribution curves displayed in Figure 2c and d. Moreover, the adsorption volume dramatically increased with the increase of KOH usage, indicating a more developed porous structure of S-PCMs. It is clear that the porosity of resultant porous carbons could be effectively controlled via KOH usage. Figure 2b showed the N_2 sorption isotherms of OMC and C-PCM samples, and both isotherms displayed the typical type I/II curves, implying the existence of micro/mesoporous structures. Meanwhile, an obvious upward tendency could be found in the relative pressure range from 0.9 to 1.0, which was attributed to the interparticle voids between the spherical carbons.¹⁹ Compared with the isotherms of OMC and C-PCM, it was hard to detect the upward tendency in the curves of S-PCMs, indicating that distinct textural transformation was caused by site-specific activation to

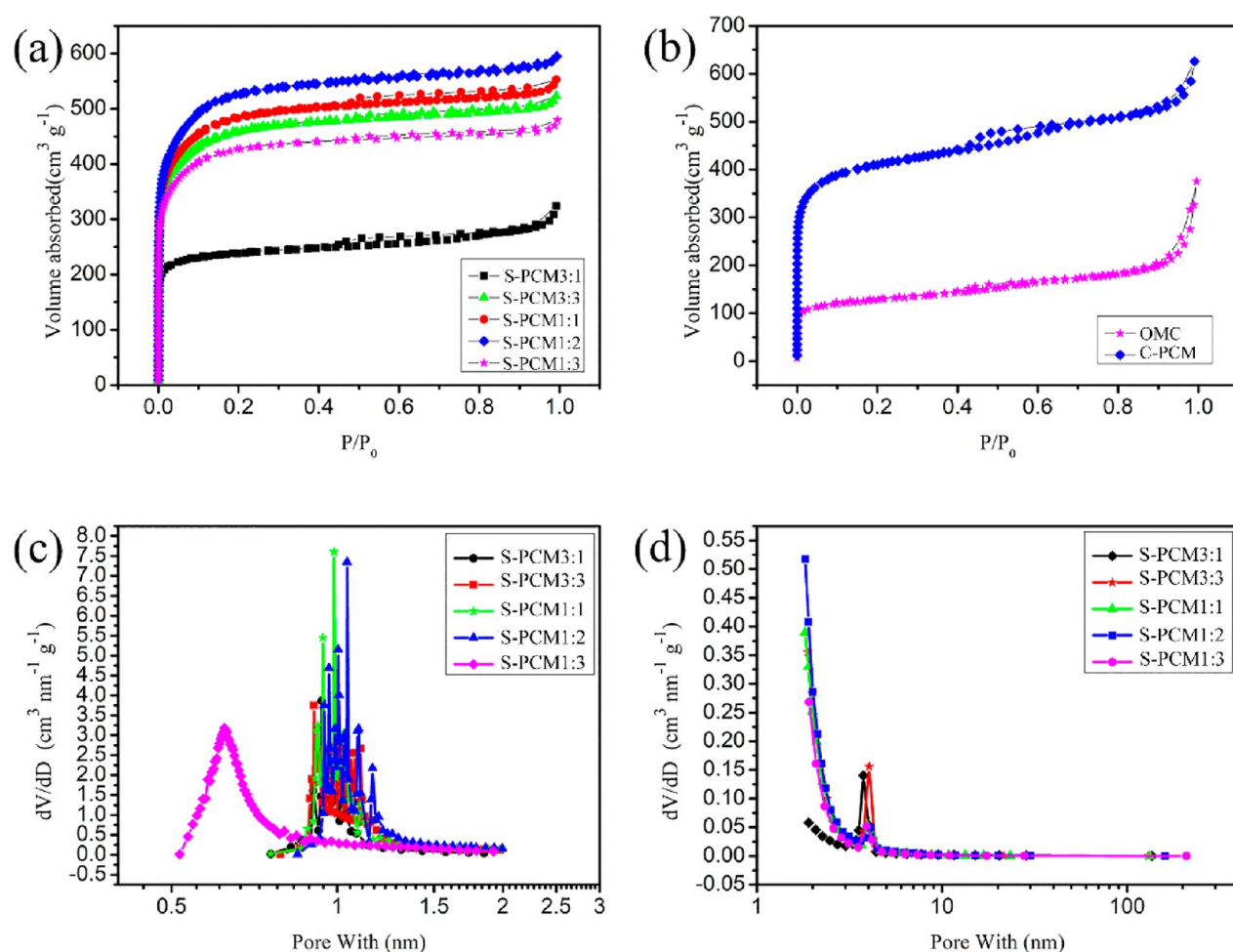


Figure 2. (a) Nitrogen adsorption–desorption isotherms of S-PCMs, (b) nitrogen adsorption–desorption isotherms of OMC and C-PCM, (c) micropore size distributions of S-PCMs via Harvath-kawazoe (HK) method, and (d) mesopore size distributions of S-PCMs via Barrett–Joyner–Halenda (BJH) method.

destroy the interparticle voids between carbon particles. The pore size distribution of the as-prepared OMC, C-PCM, and S-PCMs was presented in Figure 2c,d and Figure S9, respectively. For the mesopore distribution, all the as-prepared samples possessed mesopores with a size of 3–5 nm, which was originated from organic–organic self-assembly of phenolic resin with Pluronic F127. OMC possessed low mesoporous content because most of the mesopores produced by self-assembly in OMC was closed. Through conventional activation, the as-prepared C-PCM exhibited the highest mesoporous content due to the breakage of the mesoporous closure, demonstrating that porous structure could be improved by conventional two-step activation.^{18,20} When porous carbon was prepared by site-specific activation, the mesoporous content of the S-PCMs was increased first and then decreased. Compared with OMC, S-PCM3:1 exhibited higher mesoporous content with similar pore size of 3–5 nm, indicating that site-specific activation can also break the closure of mesoporous with slight activator dosage. When the molar ratio of phenolic hydroxyl group to KOH was increased to 3:2, the S-PCM3:2 possessed similar mesoporous content relative to S-PCM3:1. It should be noted that self-assembled mesopores as the aggregation point of site-specific activation were bound to be enlarged into macropores during activation, meaning that the mesopore content should be decreased with

increasing KOH dosage, whereas similar mesoporous content with the same size in both S-PCM3:2 and S-PCM3:1 indicated that the process of a mesopore transforming into a macropore was accompanied by unwrapping of closed mesopores, maintaining the relatively constant mesopore content under slight KOH dosage. As the ratio reached 1:1, the mesopore content of S-PCM1:1 was significantly lower than that of S-PCM3:2, indicating that the closed mesopores in carbonaceous precursor were completely broken. By further increasing the ratio to 1:2 and 1:3, the mesopore content of S-PCM1:2 and S-PCM1:3 was similar to that of S-PCM1:1, implying that the amount of mesoporous expansion into macropore reached a maximum as the ratio exceeded 1:1. The results were proven by the abrupt change of the morphology of S-PCMs from the SEM images as presented in Figure 1. Meanwhile, there was a strong difference in micropore distribution of the samples obtained from conventional activation and site-specific activation. Conventional activation had resulted in the formation of micropores with diameter of 0.6–0.8 nm accompanied by a single peak, whereas the site-specific activation led to the formation of micropore with larger diameter of 0.9–1.1 nm accompanied by multiple peaks, which could be attributed to the different positions of the phenolic hydroxyl group in the carbonaceous precursor. When porous carbon was prepared by site-specific activation, the content of

the micropore was increased gradually with the increase of activator dosage, and reached the highest value when the molar ratio of phenolic hydroxyl to KOH was 1:2. By further increasing the ratio to 1:3, the micropore distribution was shifted from 0.9 to 1.1 nm to 0.6–0.8 nm, which may be ascribed to the excessive use of KOH leading to conventional KOH activation to a certain degree. In site-specific activation, H of the hydroxyl group in the precursor was replaced by K in the process of a fixed-point reaction, which resulted in the deformation of the polymer network. This deformation was retained by the carbon skeleton to make the micropore diameter larger, leading to a larger micropore size within the range of 0.9–1.1 nm. When the dosage of KOH was much higher than that of $-C-O-K$ in the site-specific activation, such as S-PCM1:3, extra KOH would further participate in the pore-developing process after $-C-O-K$ groups in aggregated sites were consumed. Thus, the deformed carbon skeleton was first consumed by $-C-O-K$ groups, and then subsequent pore formation was carried out on the carbon skeleton in conventional activation by excessive KOH. Due to the much higher KOH dosage relative to that of site-specific activation in S-PCM1:3, the micropore size was shifted from large diameter to small diameter, demonstrating the micropore distribution characteristic of conventional carbon. The variation of porous structure would significantly influence the specific surface area of carbon materials. It has been found from Table 1 that OMC

Table 1. Textural Properties of the OMC, C-PCM, and S-PCMs Samples

| sample | pore parameters | | | |
|----------|------------------------------------------------------|--------------------------------------------|--------------------------------------------------------|---------------------------------------------------------|
| | S_{BET}^a [$\text{m}^2 \text{g}^{-1}$] | V_t^b [$\text{cm}^3 \text{g}^{-1}$] | V_{meso}^c [$\text{cm}^3 \text{g}^{-1}$] | V_{micro}^d [$\text{cm}^3 \text{g}^{-1}$] |
| OMC | 469.2 | 0.58 | 0.41 | 0.17 |
| C-PCM | 1563.8 | 0.96 | 0.36 | 0.60 |
| S-PCM3:1 | 919.7 | 0.50 | 0.17 | 0.33 |
| S-PCM3:2 | 1528.0 | 0.80 | 0.20 | 0.60 |
| S-PCM1:1 | 1733.8 | 0.85 | 0.22 | 0.63 |
| S-PCM1:2 | 1927.9 | 0.92 | 0.25 | 0.67 |
| S-PCM1:3 | 1659.0 | 0.74 | 0.11 | 0.63 |

^aBET surface area. ^bTotal pore volume. ^cMesopore volume obtained by subtracting V_{micro} from V_t . ^dMicropore volume determined by using the t -plot method.

showed the lowest specific surface area of $469.2 \text{ m}^2 \text{g}^{-1}$ and C-PCM possessed a high specific surface area of $1563 \text{ m}^2 \text{g}^{-1}$, which proved that conventional activation could significantly increase the specific surface area. However, the specific surface area can be increased more effectively and directly by site-specific activation. From Table 1, it can be observed that even the sample, S-PCM3:2, prepared by site-specific activation with KOH dosage of only 0.2 g exhibited the similar specific surface area of $1528.0 \text{ m}^2 \text{g}^{-1}$ to that of C-PCM prepared by conventional activation with 1.6 g KOH dosage. Meanwhile, S-PCM1:2 possessed the highest specific surface area of $1927 \text{ m}^2 \text{g}^{-1}$, which was 20% more than that of $1563 \text{ m}^2 \text{g}^{-1}$ for C-PCM, indicating that the specific surface area of porous carbon could be preferably improved through textural and morphological transformation by site-specific activation. Higher specific surface area directly represented faster ion or molecule transport under similar pore capacity. Based on the characteristics of large specific surface area, large pore volume, and 3D interconnected flake network, the as-prepared S-PCMs could

achieve rapid ion contact diffusion, which is more suitable for energy storage or gas adsorption applications.^{21–23}

From the results of SEM, TEM, and nitrogen adsorption/desorption, S-PCM1:1 and S-PCM1:2 were considered to be representative samples from the one-step site-specific activation for further detailed analysis. The XPS spectra of S-PCM1:1, S-PCM1:2, OMC, and C-PCM (Figure S11) showed the clear signals of carbon (285 eV), nitrogen (400 eV), oxygen (532 eV), and sulfur (167 eV) elements and the analytical results of the surface elemental content were displayed in Table S1. From Table S1, it could be seen that all four carbon materials contained a large amount of N and O elements, while the content of S elements was negligible below 1%. Compared with OMC without activation, the nitrogen content on the surface of the C-PCM was increased, which could be ascribed to the exposure of internal functional groups by activated corrosion, and the nitrogen content of S-PCMs was slightly reduced due to the reaction between KOH and hydrothermal precursors to release internal ammonia (proved by FTIR). For the oxygen element, the samples of OMC and C-PCM had similar oxygen content, while both S-PCM1:1 and S-PCM1:2 possessed higher oxygen content than that of OMC and C-PCM due to the exposure of mesopores with much phenolic hydroxyl group by site-specific activation. Due to the existence of a large quantity of N and O elements, it was necessary to further study the chemical environment of nitrogen and oxygen on the surface of the carbon materials, and the resulting high resolution N 1s and O 1s spectra were presented in Figure 3a and b. In the case of N 1s, four different peaks centered at $398.5 \pm 0.2 \text{ eV}$, $400.5 \pm 0.2 \text{ eV}$, $401.2 \pm 0.2 \text{ eV}$, and $402.9 \pm 0.2 \text{ eV}$ were detected, corresponding to pyridinic-N (N-6), pyrrolic-/pyridine-N (N-5), quaternary-N (N-Q), and pyridine-N-oxide (N-X),^{24–26} respectively. It was found that both conventional activation and site-specific activation could increase the proportion of N-5 and N-Q in N content. The increase of N-5 and N-Q in N content could be attributed to the carbon atoms next to pyridinic N which was reacted with OH species resulting in consequent transformation of the pyridinic-N (N-6) to pyrrolic-/pyridine-N (N-5).^{27,28} Meanwhile, compared with the conventional activation, the precursor in site-specific activation with excellent wettability provided better conditions to alter pyridinic-N (N-6) to pyrrolic-/pyridine-N (N-5). As a result, only pyrrolic-/pyridine-N (N-5) was the predominant species in the S-PCMs from site-specific activation as demonstrated from the peak intensities of the nitrogen species in Figure 3, which indicated that the activation degree of site-specific activation was higher than that of traditional activation. In the case of O 1s, deconvoluted O 1s spectra contained four characteristic peaks at $531.3 \pm 0.2 \text{ eV}$, $532.4 \pm 0.3 \text{ eV}$, $533.9 \pm 0.5 \text{ eV}$, and $536.3 \pm 0.2 \text{ eV}$, corresponding to $C=O$ (O-I), $C-OH/C-O-C$ (O-II), $O-C=O$ (O-III),^{29–32} respectively. It should be noted that S-PCMs and C-PCM demonstrated similar O 1s characteristic peaks indicating that the proportion of O-I and O-II in oxygen content was increased, which was attributed to the introduced oxygen during activation.^{27,28} By these results, it can be concluded that the chemical composition of the porous carbons would not change significantly by site-specific activation, and the results were similar to those of traditional activation that large amounts of N, O elements were retained in porous carbon.

3.2. Activation Mechanism. The reaction between KOH and functional groups in carbonaceous precursors on the basis

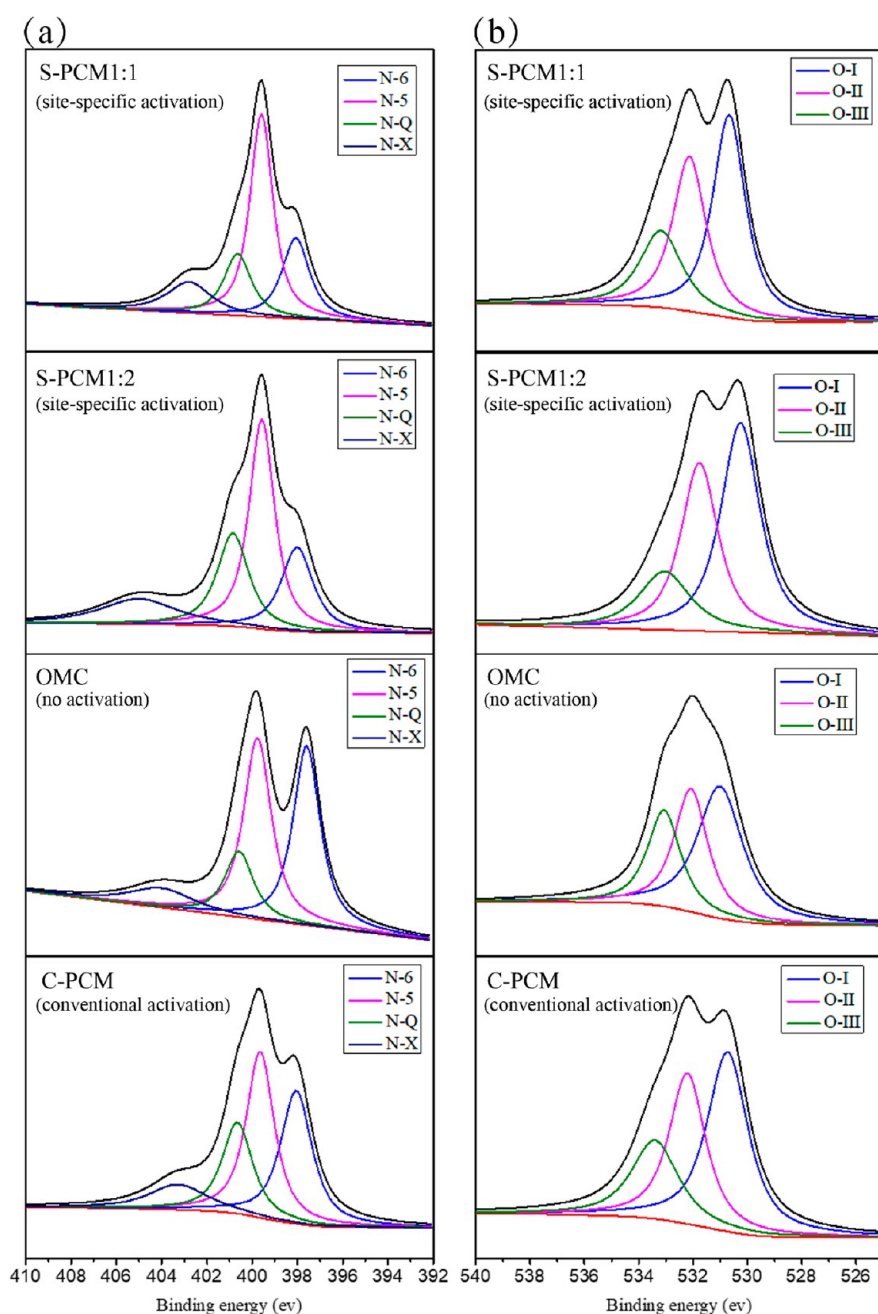


Figure 3. (a) N 1s and (b) O 1s peak-fitting XPS spectra of S-PCM1:1, S-PCM1:2, OMC, and C-PCM.

of excellent solubility was the prerequisite for the one-step site-specific activation. When the hydrothermal products serving as carbonaceous precursors were blended with aqueous KOH solution, the mixture turned from yellow to dark brown (Figure S12). In order to verify whether alkali metal elements were introduced into the carbonaceous precursor at a specific location, FTIR was used to detect the chemical variation of the precursors. It was noted that the molecular structure of hydrothermal products was changed after mixing with KOH (Figure 4). The spectra of hydrothermal products showed the peak at 1600 cm^{-1} allocated to N–H vibration and coupled with C–N tension mode,²⁴ the peak at 2880 cm^{-1} allocated as the stretching bands of C–H group,³³ and the wide band with a center of 3400 cm^{-1} designated as O–H vibration mode and N–H tension.³⁴ The high intensities of the broad absorption band at a center of 3400 cm^{-1} and the peak at 1600 cm^{-1} of

hydrothermal products indicated the existence of a great number of hydrophilic groups including hydroxyl groups and amino groups, suggesting excellent wettability with KOH. When KOH was mixed with hydrothermal products, the significant decrease in the intensity of the hydroxy absorption band at 3400 cm^{-1} was observed for the mixture. It showed that KOH was successfully reacted with phenolic hydroxyl group, which was consistent with the predesigned process. The peak at 1350 cm^{-1} attributed to C–N stretching vibration^{24,33} was not changed in the mixture. With the combination of absorption band at 1600 cm^{-1} allocated to N–H vibration and coupled with C–N tension mode, the decreased intensity at 1600 cm^{-1} could be attributed to the disappearance of the N–H bond, indicating that the N content in S-PCM was decreased by the reaction of KOH and ammonium salts, which were produced by the reaction between sulfuric acid and

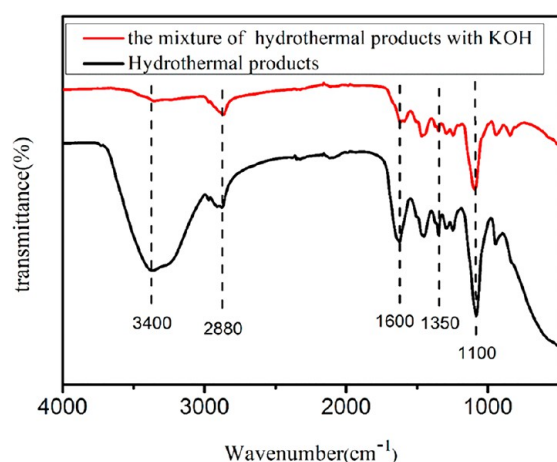


Figure 4. FTIR spectra of hydrothermal products and the mixture of hydrothermal products with KOH.

ammonia during the hydrolysis of urotropine. The intensity of the broad absorption band at 2880 cm^{-1} which represented the cross-linking degree of the product by $-\text{CH}_2-$ functional group did not change significantly after adding KOH, indicating that the addition of KOH did not significantly reduce the cross-linking degree of the resin. Thus, it could be concluded that the reaction of KOH with phenolic hydroxyl

group successfully fulfilled the site-specific requirement by the favorable wettability of hydrothermal products.

Based upon the above experimental results, a one-step site-specific activation mechanism was proposed for the formation of porous carbons derived from self-assembly hydrothermal carbonaceous precursor as illustrated in Figure 5. First, ordered assembled PF-resin was fabricated via an organic–organic self-assembly process with *m*-aminophenol as the carbon and nitrogen source and Pluronic F-127 as the soft template, which was further hydrothermally treated under mild conditions to produce the carbonaceous precursor for the subsequent activation process. The hydrothermal carbonaceous precursor displayed excellent wettability with KOH due to the existence of abundant hydrophilic groups, which could make KOH molecules enter the whole interior of the carbonaceous precursor and further react with phenol hydroxyl groups to immobilize the activators by forming the C–O–K functional group. Moreover, the ordered mesoporous structure from the PF resin self-assembly was maintained by a hydrothermal process, characterizing that the phenol hydroxyl groups were aggregated and concentrated on the pore interior of the carbonaceous precursor. The unique feature of phenol hydroxyl group aggregation provides the concentration of specific reactional sites for KOH activation, demonstrating a significant difference from other carbonaceous precursors derived from biomass,⁸ biomass derivatives,¹³ and hydro-

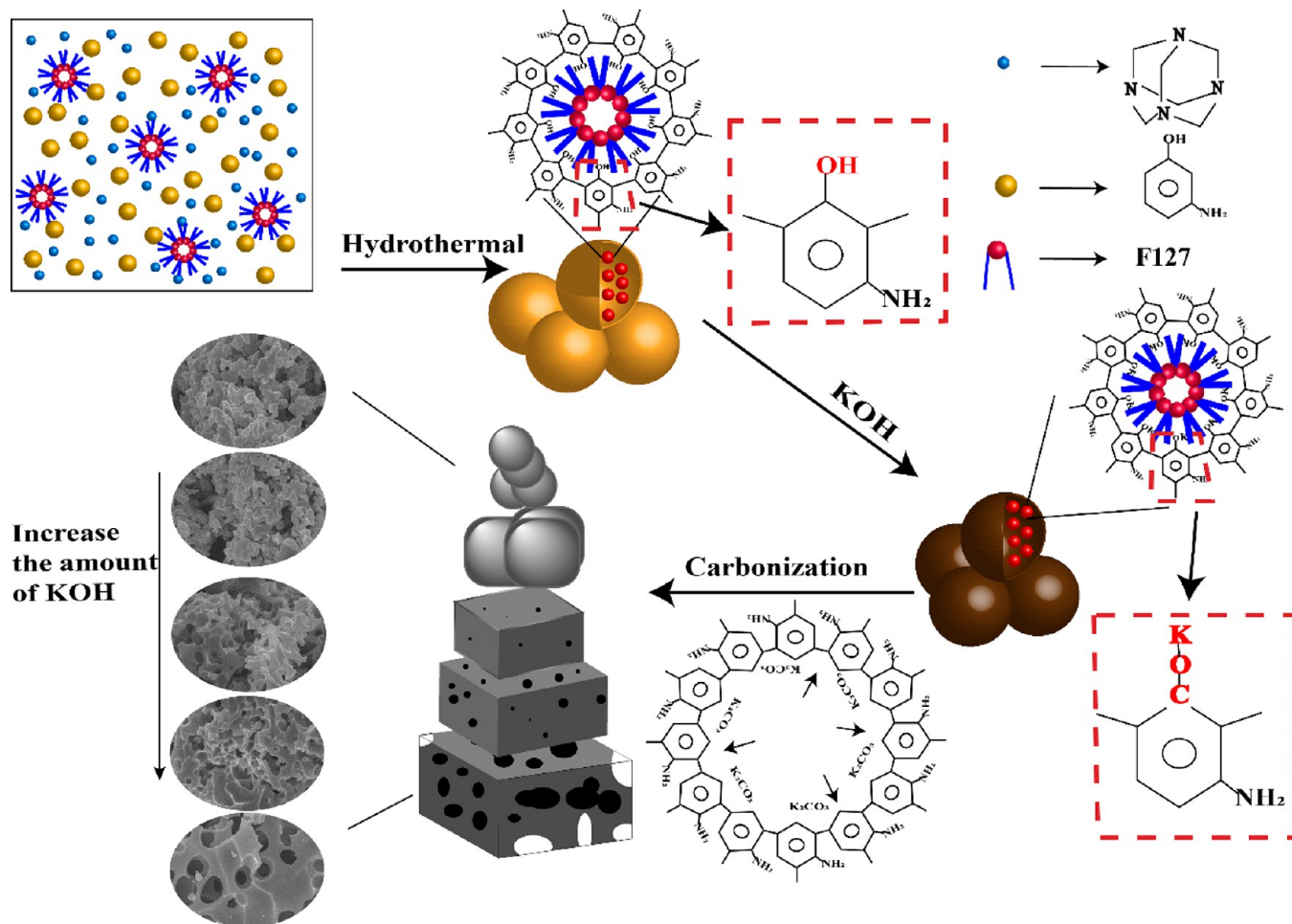


Figure 5. Schematic illustration of site-specific activation mechanism in one step for preparation of porous carbons.

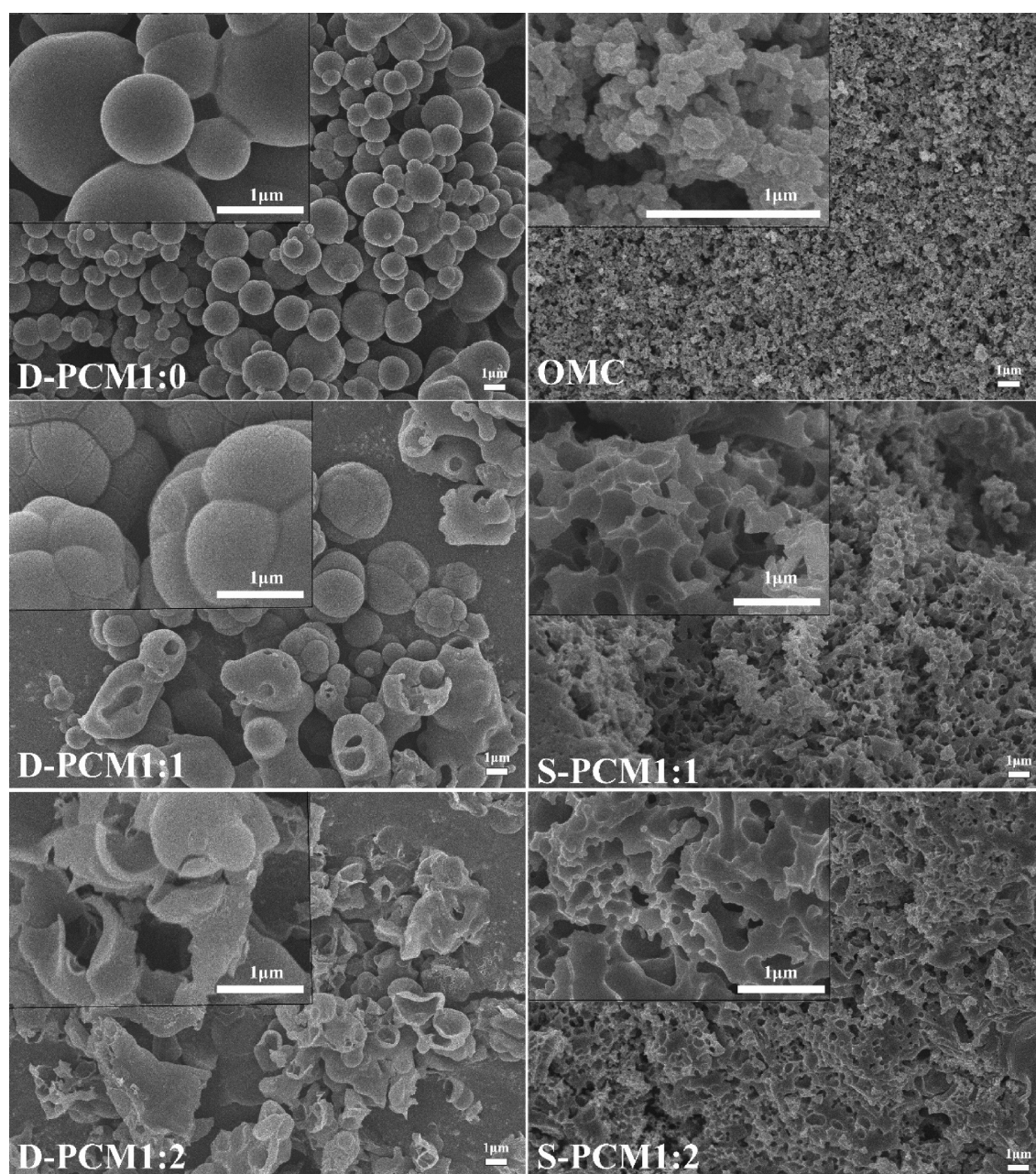


Figure 6. Contrastive SEM images of the D-OMCs from phenolic resin without Pluronic F127 (left), and PCM and S-PCMs from phenolic resin self-assembled with Pluronic F127.

thermal polymer products,³⁵ in which polar groups were randomly distributed in the precursors. Once the hydrothermal carbonaceous precursors were mixed with KOH, KOH molecules would react with phenolic hydroxyl groups to form C–O–K groups in the internal mesoporous pore of the carbonaceous precursors due to the excellent wettability of the hydrothermal precursors which could make KOH molecules enter the interior of the hydrothermal precursors. Although the C–O–K groups were formed with reversible destruction of water evaporation during drying, the aggregation of KOH in C–O–K form at the specific site was located at phenolic hydroxyl groups in the interior of the carbonaceous precursor pore.^{14,15} Calcinating the mixture of the precursor and KOH at high temperature, the C–O–K groups formed in the pore interior were decomposed to K_2CO_3 , which was further transformed to K_2O with release of CO_2 . The formation of

K_2CO_3 from C–O–K groups was conducted as the exfoliation of carbon atoms from the internal pore wall which acted like the etching of carbon by activator during conventional activation route. Simultaneously, the release of CO_2 from decomposition of K_2CO_3 to K_2O at high temperature would dilate the surrounding carbon structure acting as a pore-enlarging agent, leading to the expansive porous structure. Thus, the synergistic effect of exfoliation and expansion originating from the formation and decomposition of K_2CO_3 would remarkably promote the porous development and even transform the carbon texture, achieving activation of the carbonaceous precursor in one step by eliminating the carbonization step at high temperature which was usually carried out in conventional activation route.

Concerning the one-step activation mainly occurring at the specific sites of phenolic hydroxyl groups which was aggregated

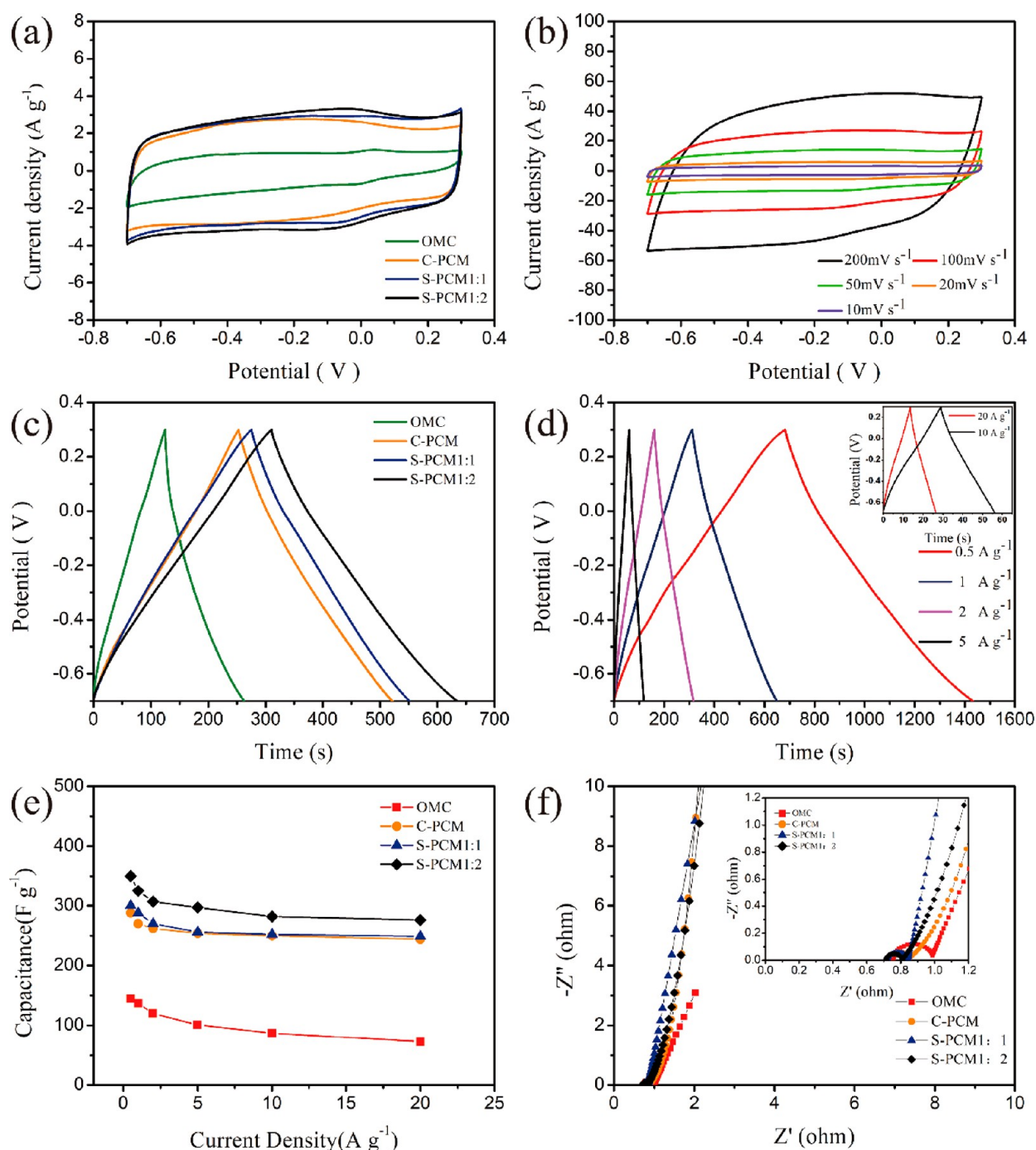


Figure 7. (a) CV curves of the OMC, C-PCM, S-PCM1:1, and S-PCM1:2 electrodes at a scan rate of 10 mV s⁻¹; (b) CV curves of the S-PCM1:2 electrodes at a scan rate from 10 mV s⁻¹ to 200 mV s⁻¹; (c) GCD curves of the OMC, C-PCM, S-PCM1:1, and S-PCM1:2 electrodes at a current density of 1 A g⁻¹; (d) GCD curves of the S-PCM1:2 at current density from 0.5 to 20 A g⁻¹; (e) charge–discharge rate performance of the OMC, C-PCM, S-PCM1:1, and S-PCM1:2 electrodes; (f) Nyquist plots of the OMC, C-PCM, S-PCM1:1, and S-PCM1:2 electrodes in the frequency range from 10⁵–10⁻² Hz (the inset is the magnified plots in the high frequency region).

by the self-assembly process, it was reasonably accepted that the carbon texture would be significantly transformed by the activated reaction with a small quantity of activators due to the location of phenolic hydroxyl groups at the interior of the precursor pores. When the reaction degree for site-specific activation was low, meaning that partial phenolic hydroxyl groups in the carbonaceous precursor were reacted with slight KOH, the porous structure of the activated carbons was obviously altered from ordered mesopores of OMC to enlarged pores and the content of mesopore at 3–5 nm was

increased due to the breakage of the mesoporous closure. Meanwhile, the micropore with diameter of 0.9–1.1 nm accompanied by special multiple peaks was formed by the site-specific activation. Although the implementation of site-specific activation significantly altered the pore structure of the carbon material, the carbon morphology was kept as coral-like particles only with slightly larger size due to the low degree of reactivity (S-PCM3:1 and S-PCM3:2 in Figure 1). Increasing the reaction degree up to the point that all the phenolic hydroxyl groups were reacted with equivalent or

slightly excessive KOH (S-PCM1:1 and S-PCM1:2 in Figure 1), not only was the pore texture dramatically transformed, but the morphology of the porous carbon was as well. The content of micropore in the porous carbons was increased with the increase of site-specific reaction degree and the micropore distribution still retained multipeak distribution in the range of 0.9–1.1 nm. However, because of the aggregation of specific reactive sites, the mesopore content in the porous carbons was reduced through the transformation of the inner mesopore into the outer wall of carbons by activation. Furthermore, the morphology was accordingly transferred from coral-like spherical particles into a 3D interconnected network or even a 3D interconnected flake network due to pore transformation. When the amount of KOH was much higher than that of phenolic hydroxyl group (S-PCM1:3 in Figure 1), the mesopore distribution was kept constant, but the micropore distribution was shifted from 0.9 to 1.1 nm to 0.6–0.8 nm. Meanwhile, the morphology of the interconnected 3D flake network was further developed by reducing the thickness of the wall of carbon material. Despite dramatic alteration on the morphology and porous structure of the carbons prepared by site-specific activation, two weak and broad diffraction bands centered at 23.4° and 43° were still maintained in S-PCMs, which can be approximately indexed as the (002) and (101) plane of graphite structure (Figure S10).^{36,37}

In order to demonstrate the effect of the predesigned expansion from aggregated specific sites on a porous structure, the site-specific activation was performed on phenolic resin as a carbonaceous precursor with and without Pluronic F127, respectively. The contrasting SEM images of the as-prepared activated samples from phenolic resin without Pluronic F127 labeled as D-OMC and that from phenolic resin self-assembled with Pluronic F127 as S-PCM were presented in Figure 6. For the D-OMC sample obtained from direct carbonization without KOH activation, it was mainly composed of spherical carbon particles, which was different from the small coral-like interconnected particles in OMC. After site-specific activation under the molar ratio of 1:1, the as-prepared D-OMC1:1 almost kept the original spherical particles with a small amount of amorphous carbons, which was a lack of the remarkable morphological variation with comparison to S-PCM1:1. By increasing KOH dosage to the ratio 1:2, amorphous carbons featured with broken flakes were formed in D-OMC1:2, indicating that the irregular expansion of porous structure occurred in a random way and further altered the morphology through breaking up the regular particles. However, different from the transformation of porous structure and morphology of S-PCM, the irregular distribution of phenolic hydroxyl groups in D-OMC could not alter the morphology in the predesigned way, leading to the amorphous morphology of the carbons. On the contrary, both the morphology and the porous structure of S-PCM could be converted in the predesigned way by aggregation of reactive groups in special parts of the carbonaceous precursor. Through the site-specific activation, precise and controllable activation could be realized by regulating the distribution of reaction sites.

It could be apparent to improve the porosity and surface area of the carbon materials by the conventional two-step activation method. The prepared C-PCM sample possessed larger specific surface area and pore volume than that of OMC sample, still maintaining similar morphology and porous texture after annealing OMC with massive KOH (in the mass ratio of 4:1, KOH to OMC) at high temperature.

However, only by aggregating the specific sites on the internal pores previously assembled in the carbonaceous precursors could the porosity, texture, and morphology of the activated carbon materials be significantly transformed by a small amount of KOH dosage. Although the reaction between KOH and phenolic hydroxyl groups has not been intrinsically changed, the aggregation of reactive sites resulted in the remarkable conversion of products from spherical particles to a 3D interconnected flake network, bringing about high specific surface area that was comparative or even preferable to that conventional activation. Moreover, the porous and morphological evolution could be conducted in a consecutive way with slight KOH dosage, demonstrating excellent control over the porosity, pore size distribution, and morphology of the activated porous carbons. In addition, the site-specific activation approach was also different from other one-step activation methods which were carried out by direct calcination of carbonaceous precursor and activator mixtures.^{8,10,34,38} Even though one-step activation procedure was performed based on the reaction of activators including KOH with hydrophilic polar groups, the randomly distributed reactive groups in carbonaceous precursor led to limited control over pore type and pore size distribution, and still required a massive dosage of activators with equivalent to that used in the conventional two-step activation process. Taken together, by a simple directional arrangement of special functional groups of carbonaceous precursors, porous carbons with high specific surface area and controllable porosity could be prepared through a cost-effective and environmentally friendly way.

3.3. Electrochemical Properties. The electrochemical properties of the porous carbons obtained from one-step site-specific activation were conducted by CV, GCD, and EIS measurements with a three-electrode system in 1 M H_2SO_4 electrolyte. Figure 7a showed the CV curves of different carbon materials at a scan rate of 10 mV s^{-1} . The PCM, NO-PCM, and T-PCMs displayed a typical rectangular shape, indicating the electric double-layer capacitive response.³⁹ In addition, certain slight humps could be observed in all samples, suggesting that the pseudocapacitance caused by redox reactions was related to the heteroatom doping.⁴⁰ The CV curve of S-PCM1:2 enclosed the largest area, indicating the largest specific capacitance of S-PCM1:2 at the same rate. Furthermore, Figure 7b exhibited the CV curves of S-PCM1:2 at different rates from 10 mV s^{-1} to 200 mV s^{-1} . The CV profiles of S-PCM1:2 showed a rectangular shape at 200 mV s^{-1} , indicating a very fast electrochemical response.^{41,42} Figure 7c further presented the GCD curves of all the samples at the same current density of 1 A g^{-1} , and all the GCD curves exhibited similar isosceles triangle arc, revealing that the capacitance response mainly came from the double-layer capacitance, and the electrodes exhibited good electrochemical reversibility. Meanwhile, S-PCM1:2 showed the longest charging and discharging time, which indicated that S-PCM1:2 possessed the highest specific capacitance at the same current density of 1 A g^{-1} that was in accordance with Figure 7a. The charge and discharge performance of S-PCM1:2 at different current densities were measured separately and shown in Figure 7d. All the charge–discharge curves resembled an isosceles triangle, and no deformation of charge–discharge curves even at high current density of 20 A g^{-1} . Figure 7e displayed a plot of the specific capacitance as a function of the current density. It could be found that the

specific capacitance was decreased by increasing the current density. S-PCM1:2 displayed the highest specific capacitance at the same current density (the specific capacitance was 375 F g⁻¹ at the current density of 0.5 A g⁻¹ and 276 F g⁻¹ at the current density of 20 A g⁻¹, 74% capacitance retention) compared to other samples under the same conditions (the specific capacitance values for C-PCM was 288 F g⁻¹ at the current density of 0.5 A g⁻¹ and 242 F g⁻¹ at the current density of 20 A g⁻¹, 84% capacitance retention), suggesting a much higher rate capability compared with that of various porous carbons previously reported as listed in Table 2.

Table 2. Summary of Electrochemical Performance of Porous Carbons in Recent Literature

| carbon material | capacitance (F g ⁻¹) | rate performance | electrolyte | ref |
|-----------------------------------------|----------------------------------|-------------------------------------------------|------------------------------------|-----------|
| N-doped holey graphene aerogel | 318.3 (0.5 A g ⁻¹) | 259.6 F g ⁻¹ at 20 A g ⁻¹ | 6 M KOH | 43 |
| N-doped carbon nanospheres | 376 (0.5 A g ⁻¹) | 130 F g ⁻¹ at 20 A g ⁻¹ | 6 M KOH | 44 |
| N/P codoped graphene | 219 (0.25 A g ⁻¹) | 175 F g ⁻¹ at 10 A g ⁻¹ | 6 M KOH | 45 |
| Porous carbon/carbon nanotube composite | 324 (0.5 A g ⁻¹) | 152 F g ⁻¹ at 10 A g ⁻¹ | 6 M KOH | 46 |
| N-doped carbon | 278 (0.2 A g ⁻¹) | 147 F g ⁻¹ at 10 A g ⁻¹ | 1 M H ₂ SO ₄ | 47 |
| Graphene aerogel | 306 (0.1 A g ⁻¹) | 215 at 4 A g ⁻¹ | 2 M H ₂ SO ₄ | 48 |
| Activated carbon | 226 (1 A g ⁻¹) | 206 at 10 A g ⁻¹ | 6 M KOH | 9 |
| Site-specific-activated porous carbon | 375 (0.5 A g ⁻¹) | 276 at 20 A g ⁻¹ | 1 M H ₂ SO ₄ | This work |

The variation of morphology and porous structure exerted a significant impact on ion transport, which could be directly reflected by EIS plot (Figure 7f). It could be observed that all EIS curves of the samples possessed three sections: the nearly vertical lines in a low frequency region, the 45° diagonal line in the intermediate frequency region, and the semicircle in the high frequency region. The difference was mainly focused on the part in the high-frequency semicircle, in which the semicircle in the high-to-medium frequency region corresponded to the charge transfer resistance (R_{ct}), and the semicircle diameter reflected the magnitude of R_{ct} . It could be found that the as-prepared samples including C-PCM and S-PCMs after activation exhibited smaller semicircle diameter than that of OMC without activation, demonstrating that higher effective contact area in porous carbon through activation was achieved for rapid electrolyte ion transfer.^{49,50} The fact that high effective contact area from the activated carbons proved that the comparative or even preferable activation effect could be achieved by the site-specific activation method with small KOH dosage compared with a conventional two-step activation route. For example, S-PCM1:2 displayed only two-thirds of the diameter of other activated samples, indicating much faster electrolyte ion transfer. It was mainly attributed to the morphological transformation of the porous carbon to 3D sheet interconnection network, which possessed a higher effective contact area than that of coral-shaped carbon. In the intermediate frequency region, the 45° diagonal line, called the Warburg curve, was representative of the diffusion of electrolyte ions within porous electrodes. The projected length of the Warburg curve on the real impedance axis (Z_{re}) characterized the ion diffusion

resistance.²⁷ It could be found that the property of ion diffusion of C-PCM and S-PCMs was better than that of OMC, which was attributed to the active pore-forming and pore-opening effect. Compared with C-PCM, S-PCM had a slightly larger ion diffusion resistance, because the mesoporous which accelerated the kinetic process of ion diffusion were destroyed by site-specific activation.^{51,52} Meanwhile, the morphological transformation of the porous carbon to 3D sheet interconnection network increased the bending degree of the material, which had a certain effect on ion diffusion, and S-PCM1:2 showed relatively large ion diffusion resistance.⁵¹ The vertical line in the low frequency region means an ideal capacitive property. It could be found that the slope of the vertical line of C-PCM and S-PCMs was closer to 90° than that of OMC after activation, indicating that C-PCM and S-PCMs had better capacitive property with a large number of micro-/mesoporous.⁵² On the whole, the highly hierarchical structure of the 3D sheet interconnected carbon rendered high utilization of the micro-, meso-, and macropores in favorable electrochemical behavior, which has been reported and proven in a specific way that the massive micropores accessible to the electrolyte ions was beneficial for high energy storage, mesopores accelerated the kinetic process of ion diffusion in the electrodes for improving the power performance at high current densities, and macropores provided a short diffusion distance and facilitated rapid transport of electrolyte ions, and hence resulting in the superior capacitive performance.^{10,53–56}

The porous carbons from site-specific activation in one step possessed high specific surface area, well-defined hierarchical pores, and appropriate porous distribution, which could guarantee good performance when used as supercapacitors. A symmetric supercapacitor was assembled by S-PCM1:2 and the electrochemical performance was explored as shown in Figure 8. Figure 8a exhibited CV curves of the supercapacitor at various scanning rates from 5 to 200 mV s⁻¹ in 1 M H₂SO₄ electrolyte. The CV profiles showed a nearly perfect rectangular shape and no distortion at high sweep rates of 200 mV s⁻¹, indicating a small equivalent series resistance (ESR) and an excellent capacitive nature.³⁹ The GCD curves of S-PCM1:2 at different current densities in 1 M H₂SO₄ electrolyte were displayed in Figure 8b. The galvanostatic charge/discharge profiles demonstrated almost symmetric triangular shapes, revealing good capacitive characteristics and electrochemical reversibility. The specific capacitance was reduced from 281 to 225 F g⁻¹ as the current density increased from 0.5 to 20 A g⁻¹, retaining about 81% of the initial capacitance, which was indicative of an excellent rate performance of S-PCM1:2. The performance was significantly higher than that of other synthetic porous carbon materials, such as template-free synthesis of N-doped carbon⁵⁷ (256 F g⁻¹ at 0.5 A g⁻¹ and 183 F g⁻¹ at 20 A g⁻¹), 3D microporous conducting carbon⁵⁸ (254 F g⁻¹ at 0.5 A g⁻¹ and 150 F g⁻¹ at 30 A g⁻¹), and 3D self-assembly synthesis of hierarchical porous carbon⁵⁹ (277 F g⁻¹ at 0.05 A g⁻¹ and 194 F g⁻¹ at 20 A g⁻¹). The EIS profile (Figure 8c) exhibited a semicircle in the middle and high frequency region, and a nearly perpendicular line in the low-frequency region, indicating the outstanding ionic and electronic conductivity of S-PCM1:2. Figure S13 depicted the Ragone plot related to energy and power densities of the symmetric supercapacitor using 1 M H₂SO₄ solution as the electrolyte. Profiting from high utilization of the micro-, meso-, and macropores in favorable electrochemical behavior, the energy density of the symmetric

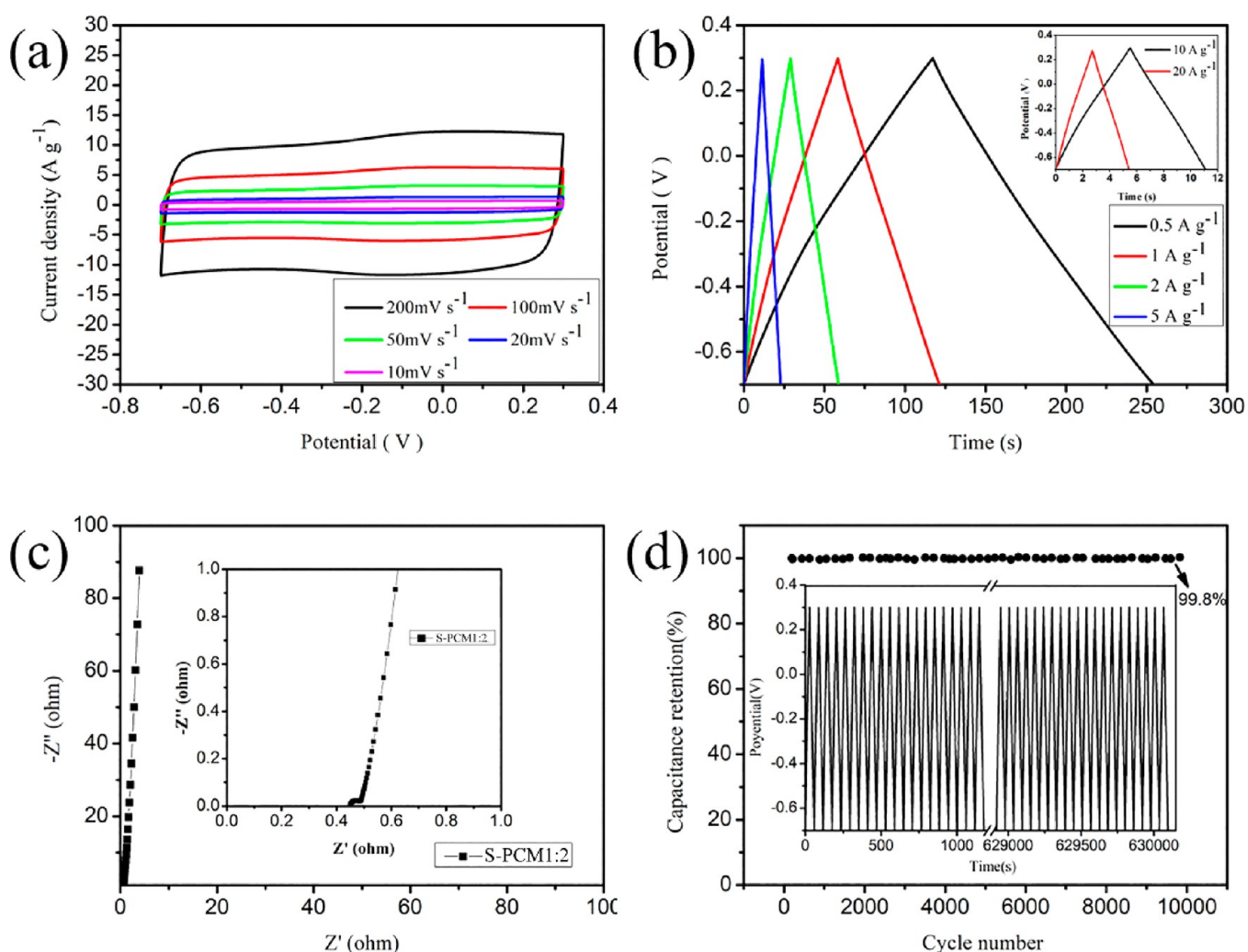


Figure 8. Electrochemical performance of NOS-PCMs-700//NOS-PCMs-700 symmetric supercapacitors (a) CV curves of the S-PCM1:2 at a scan rate from 10 to 200 mV s⁻¹; (b) GCD curves of the S-PCM1:2 at current density from 0.5 to 20 A g⁻¹; (c) Nyquist plots of the S-PCM1:2 in the frequency range from 10⁵ to 10⁻² Hz (the inset is the magnified plots in the high frequency region); (d) cycling performance of S-PCM1:2 at 2 A g⁻¹ in 1 M H₂SO₄ electrolyte, is the GCD curves for the first and last 20 cycles.

cell exhibited 9.72 W h kg⁻¹ at a current density of 0.5 A g⁻¹ and remained at 7.81 W h kg⁻¹ with a power density of 9600 W kg⁻¹ at 20 A g⁻¹, which was significantly higher than other one-step activation porous carbon or synthetic porous carbon at high power density.^{10,14,58,60,61} Based on the above electrochemical property, the cycles of symmetrical supercapacitor S-PCM1:2//S-PCM1:2 were tested at long cycle current densities of 2 A g⁻¹. After 10 000 cycles of charging and discharging, the capacitance retention rate was about 99.8% of the initial specific capacitance at 2 A g⁻¹ in 1 M H₂SO₄ electrolyte, evidencing the outstanding cycling stability and relatively high reversibility of the S-PCM1:2. The above experimental results demonstrated that S-PCM1:2 displayed excellent electrochemical performance, which was mainly attributed to the hierarchical porosity with high specific surface area and large micropore volume. The distinctive morphology and porosity originated from site-specific activation, providing large electrode/electrolyte interface to form electric double layers and low-resistant pathways for rapid ion transportation among the pores.

4. CONCLUSION

Highly hierarchical porous carbons with controllable morphology and porous texture were successfully synthesized by site-specific activation in one step. Based upon the hydrophilicity of the carbonaceous precursor, the activator was introduced into the specific active hydroxyl sites in phenolic resin through the connection of C–O–K originated from the reaction of phenolic hydroxyl group with KOH. Through aggregation of specific sites in the predesigned way, the control over activated sites and entire activation was significantly improved, resulting in dramatic morphological evolution of the as-prepared porous carbon from coral-like particle to 3D sheet interconnection network. Different from the conventional two-step activation method, the site-specific activation strategy was carried out not only in one step of calcination but for much lower dosage of activators. The S-PCMs materials obtained from one-step site-specific activation exhibited the characteristics of large surface area with hierarchical porosity as well as an abundant amount of nitrogen, oxygen, and sulfur functional groups. Benefiting from the unique morphological and textural feature, the S-PCMs demonstrated excellent electrochemical performance as electrode materials for supercapacitors. The typical S-PCM1:2

exhibited an excellent specific capacitance of 276 F g⁻¹ at high current density of 20 A g⁻¹ as well as good rate performance (74% capacitance retention, 375 F g⁻¹ at 0.5 A g⁻¹) in three-electrode system. The symmetric supercapacitor assembled by S-PCM1:2 possessed a high specific energy of 7.81 Wh kg⁻¹ at power density of 9600 W kg⁻¹. Furthermore, the electrode displayed outstanding cycling stability with only 0.2% loss after 10 000 cycles.

■ ASSOCIATED CONTENT

● Supporting Information

The Supporting Information is available free of charge at <https://pubs.acs.org/doi/10.1021/acsaem.9b01729>.

Pictures of the symmetric supercapacitor device; SEM and TEM images; pore size distribution; XPS patterns; XRD patterns; pictures of hydrothermal products and the mixture of hydrothermal products with KOH; Ragone plots of S-PCM1:2 based symmetric supercapacitors in 1 M H₂SO₄ electrolyte; Elementary composition of prepared materials from XPS (PDF)

■ AUTHOR INFORMATION

Corresponding Authors

*E-mail: lixiaoli0903@163.com (Xiaoli Li).

*E-mail: lizgmse@nefu.edu.cn (Zhiguo Li).

ORCID

Zongze Lv: 0000-0002-4619-386X

Zhiguo Li: 0000-0002-2455-5153

Notes

The authors declare no competing financial interest.

■ ACKNOWLEDGMENTS

We gratefully acknowledge the support of this research work by the Fundamental Research Funds for the Central Universities (2572017CB27 and 2572017DB06), National Natural Science Foundation of China (31570557), Science Foundation of Heilongjiang Province of China (C2018008), Postdoctoral Scientific Research Developmental Fund of Heilongjiang Province (LBH-Q14004).

■ REFERENCES

- (1) Sun, X.; Zhang, Y.; Song, P.; Pan, J.; Zhuang, L.; Xu, W.; Xing, W. Fluorine-Doped Carbon Blacks: Highly Efficient Metal-Free Electrocatalysts for Oxygen Reduction Reaction. *ACS Catal.* **2013**, *3* (8), 1726–1729.
- (2) Singh, S. P.; Li, Y.; Zhang, J.; Tour, J. M.; Arnusch, C. J. Sulfur-Doped Laser-Induced Porous Graphene Derived from Polysulfone-Class Polymers and Membranes. *ACS Nano* **2018**, *12* (1), 289–297.
- (3) Kiciński, W.; Szala, M.; Bystrzejewski, M. Sulfur-Doped Porous Carbons: Synthesis and Applications. *Carbon* **2014**, *68*, 1–32.
- (4) Benziger, M. R.; Talapaneni, S. N.; Joseph, S.; Ramadass, K.; Singh, G.; Scaranto, J.; Rapon, U.; Al-Bahily, K.; Vinu, A. Recent Advances in Functionalized Micro and Mesoporous Carbon Materials: Synthesis and Applications. *Chem. Soc. Rev.* **2018**, *47* (8), 2680–2721.
- (5) Deng, J.; Li, M.; Wang, Y. Biomass-Derived Carbon: Synthesis and Applications in Energy Storage and Conversion. *Green Chem.* **2016**, *18* (18), 4824–4854.
- (6) Yan, J.; Wang, Q.; Wei, T.; Fan, Z. Recent Advances in Design and Fabrication of Electrochemical Supercapacitors with High Energy Densities. *Adv. Energy Mater.* **2014**, *4* (4), 1300816.
- (7) Wei, L.; Sevilla, M.; Fuertes, A. B.; Mokaya, R.; Yushin, G. Polypyrrole-Derived Activated Carbons for High-Performance Elec-

trical Double-Layer Capacitors with Ionic Liquid Electrolyte. *Adv. Funct. Mater.* **2012**, *22* (4), 827–834.

- (8) Fuertes, A. B.; Sevilla, M. High-Surface Area Carbons from Renewable Sources with a Bimodal Micro-Mesoporosity for High-Performance Ionic Liquid-Based Supercapacitors. *Carbon* **2015**, *94*, 41–52.
- (9) Zhang, L.; Gu, H.; Sun, H.; Cao, F.; Chen, Y.; Chen, G. Z. Molecular Level One-Step Activation of Agar to Activated Carbon for High Performance Supercapacitors. *Carbon* **2018**, *132*, 573–579.
- (10) Deng, J.; Xiong, T.; Xu, F.; Li, M.; Han, C.; Gong, Y.; Wang, H.; Wang, Y. Inspired by Bread Leavening: One-Pot Synthesis of Hierarchically Porous Carbon for Supercapacitors. *Green Chem.* **2015**, *17* (7), 4053–4060.
- (11) Lu, H.; Zhao, X. S. Biomass-Derived Carbon Electrode Materials for Supercapacitors. *Sustain. Energy Fuels* **2017**, *1* (6), 1265–1281.
- (12) Biswal, M.; Banerjee, A.; Deo, M.; Ogale, S. From Dead Leaves to High Energy Density Supercapacitors. *Energy Environ. Sci.* **2013**, *6* (4), 1249–1259.
- (13) Pang, J.; Zhang, W.; Zhang, J.; Cao, G.; Han, M.; Yang, Y. Facile and Sustainable Synthesis of Sodium Lignosulfonate Derived Hierarchical Porous Carbons for Supercapacitors with High Volumetric Energy Densities. *Green Chem.* **2017**, *19* (16), 3916–3926.
- (14) Zhou, J.; Shen, H.; Li, Z.; Zhang, S.; Zhao, Y.; Bi, X.; Wang, Y.; Cui, H.; Zhuo, S. Porous Carbon Materials with Dual N, S-Doping and Uniform Ultra-Microporosity for High Performance Supercapacitors. *Electrochim. Acta* **2016**, *209*, 557–564.
- (15) Zhou, J.; Li, Z.; Xing, W.; Zhu, T.; Shen, H.; Zhuo, S. N-Doped Microporous Carbons Derived from Direct Carbonization of K⁺-Exchanged Meta-Aminophenol-Formaldehyde Resin for Superior CO₂ Sorption. *Chem. Commun.* **2015**, *51* (22), 4591–4594.
- (16) Ma, T. Y.; Liu, L.; Yuan, Z. Y. Direct Synthesis of Ordered Mesoporous Carbons. *Chem. Soc. Rev.* **2013**, *42* (9), 3977–4003.
- (17) Górka, J.; Zawislak, A.; Choma, J.; Jaroniec, M. KOH Activation of Mesoporous Carbons Obtained by Soft-Templating. *Carbon* **2008**, *46* (8), 1159–1161.
- (18) Liu, S.; Zuo, P.; Wang, Y.; Li, X.; Zhang, W.; Xu, S.; Huo, P.; Li, Z. Nitrogen-Doped Ordered Mesoporous Carbon Microspheres Made from m-Aminophenol-Formaldehyde Resin as Promising Electrode Materials for Supercapacitors. *Microporous Mesoporous Mater.* **2018**, *259*, 54–59.
- (19) Su, F.; Chee, A.; Poh, K.; Xu, G.; Dan, W.; Qin, L.; Lin, J.; Chen, J. S.; Lou, X. W. Nitrogen-Containing Microporous Carbon Nanospheres with Improved Capacitive Properties. *Energy Environ. Sci.* **2011**, *4* (3), 717–724.
- (20) Liu, S.; Chen, X.; Li, X.; Huo, P.; Wang, Y.; Bai, L.; Zhang, W.; Niu, M.; Li, Z. Nitrogen- and Oxygen-Containing Micro-Mesoporous Carbon Microspheres Derived from m-Aminophenol Formaldehyde Resin for Supercapacitors with High Rate Performance. *RSC Adv.* **2016**, *6* (92), 89744–89756.
- (21) Wu, Z. S.; Sun, Y.; Tan, Y. Z.; Yang, S.; Feng, X.; Müllen, K. Three-Dimensional Graphene-Based Macro- and Mesoporous Frameworks for High-Performance Electrochemical Capacitive Energy Storage. *J. Am. Chem. Soc.* **2012**, *134* (48), 19532–19535.
- (22) Chmiola, J. Anomalous Increase in Carbon Capacitance at Pore Sizes Less Than 1 Nanometer. *Science* **2006**, *313* (5794), 1760–1763.
- (23) Largeot, C.; Portet, C.; Chmiola, J.; Taberna, P. L.; Gogotsi, Y.; Simon, P. Relation between the Ion Size and Pore Size for an Electric Double-Layer Capacitor. *J. Am. Chem. Soc.* **2008**, *130* (9), 2730–2731.
- (24) Raymundo-Pinero, E.; Cazorla-Amorós, D.; Linares-Solano, A. The Role of Different Nitrogen Functional Groups on the Removal of SO₂ from Flue Gases by N-Doped Activated Carbon Powders and Fibres. *Carbon* **2003**, *41* (10), 1925–1932.
- (25) Cheng, Y.; Huang, L.; Xiao, X.; Yao, B.; Yuan, L.; Li, T.; Hu, Z.; Wang, B.; Wan, J.; Zhou, J. Flexible and Cross-Linked N-Doped Carbon Nanofiber Network for High Performance Freestanding Supercapacitor Electrode. *Nano Energy* **2015**, *15*, 66–74.

- (26) Li, Z.; Xu, Z.; Tan, X.; Wang, H.; Holt, C. M. B.; Stephenson, T.; Olsen, B. C.; Mitlin, D. Mesoporous Nitrogen-Rich Carbons Derived from Protein for Ultra-High Capacity Battery Anodes and Supercapacitors. *Energy Environ. Sci.* **2013**, *6* (3), 871–878.
- (27) He, S.; Zhang, C.; Du, C.; Cheng, C.; Chen, W. High Rate-Performance Supercapacitor Based on Nitrogen-Doped Hollow Hexagonal Carbon Nanoprism Arrays with Ultrathin Wall Thickness in Situ Fabricated on Carbon Cloth. *J. Power Sources* **2019**, *434*, 226701.
- (28) Guo, D.; Shibuya, R.; Akiba, C.; Saji, S.; Kondo, T.; Nakamura, J. Active Sites of Nitrogen-Doped Carbon Materials for Oxygen Reduction Reaction Clarified Using Model Catalysts. *Science* **2016**, *351* (6271), 361–366.
- (29) Fang, Y.; Luo, B.; Jia, Y.; Li, X.; Wang, B.; Song, Q.; Kang, F.; Zhi, L. Renewing Functionalized Graphene as Electrodes for High-Performance Supercapacitors. *Adv. Mater.* **2012**, *24* (47), 6348–6355.
- (30) Kulkarni, S. B.; Patil, U. M.; Shackery, L.; Sohn, J. S.; Lee, S.; Park, B.; Jun, S. High-Performance Supercapacitor Electrode Based on a Polyaniline Nanofibers/3D Graphene Framework as an Efficient Charge Transporter. *J. Mater. Chem. A* **2014**, *2* (14), 4989–4998.
- (31) Ye, F.; Zhao, B.; Ran, R.; Shao, Z. Facile Mechanochemical Synthesis of Nano SnO₂/Graphene Composite from Coarse Metallic Sn and Graphite Oxide: An Outstanding Anode Material for Lithium-Ion Batteries. *Chem. - Eur. J.* **2014**, *20* (14), 4055–4063.
- (32) Frackowiak, E.; Béguin, F. Carbon Materials for the Electrochemical Storage of Energy in Capacitors. *Carbon* **2001**, *39* (6), 937–950.
- (33) Liu, N.; Yin, L.; Wang, C.; Zhang, L.; Lun, N.; Xiang, D.; Qi, Y.; Gao, R. Adjusting the Texture and Nitrogen Content of Ordered Mesoporous Nitrogen-Doped Carbon Materials Prepared Using SBA-15 Silica as a Template. *Carbon* **2010**, *48* (12), 3579–3591.
- (34) Hao, G. P.; Li, W. C.; Qian, D.; Lu, A. H. Rapid Synthesis of Nitrogen-Doped Porous Carbon Monolith for CO₂ Capture. *Adv. Mater.* **2010**, *22* (7), 853–857.
- (35) Zheng, X.; Lv, W.; Tao, Y.; Shao, J.; Zhang, C.; Liu, D.; Luo, J.; Wang, D. W.; Yang, Q. H. Oriented and Interlinked Porous Carbon Nanosheets with an Extraordinary Capacitive Performance. *Chem. Mater.* **2014**, *26* (23), 6896–6903.
- (36) Stobinski, L.; Lesiak, B.; Malolepszy, A.; Mazurkiewicz, M.; Mierzwa, B.; Zemek, J.; Jiricek, P.; Bieloshapka, I. Graphene Oxide and Reduced Graphene Oxide Studied by the XRD, TEM and Electron Spectroscopy Methods. *J. Electron Spectrosc. Relat. Phenom.* **2014**, *195*, 145–154.
- (37) Zhao, X.; Hayner, C. M.; Kung, M. C.; Kung, H. H. Flexible Holey Graphene Paper Electrodes with Enhanced Rate Capability for Energy Storage Applications. *ACS Nano* **2011**, *5* (11), 8739–8749.
- (38) Wang, J.; Senkovska, I.; Kaskel, S.; Liu, Q. Chemically Activated Fungi-Based Porous Carbons for Hydrogen Storage. *Carbon* **2014**, *75*, 372–380.
- (39) Liu, H.-J.; Wang, J.; Wang, C.-X.; Xia, Y.-Y. Ordered Hierarchical Mesoporous/Microporous Carbon Derived from Mesoporous Titanium-Carbide/Carbon Composites and Its Electrochemical Performance in Supercapacitor. *Adv. Energy Mater.* **2011**, *1* (6), 1101–1108.
- (40) Zhou, M.; Pu, F.; Wang, Z.; Guan, S. Nitrogen-Doped Porous Carbons through KOH Activation with Superior Performance in Supercapacitors. *Carbon* **2014**, *68*, 185–194.
- (41) Liang, Y.; Liu, H.; Li, Z.; Fu, R.; Wu, D. In Situ Polydopamine Coating-Directed Synthesis of Nitrogen-Doped Ordered Nanoporous Carbons with Superior Performance in Supercapacitors. *J. Mater. Chem. A* **2013**, *1* (48), 15207–15211.
- (42) Liang, Y.; Liang, F.; Zhong, H.; Li, Z.; Fu, R.; Wu, D. An Advanced Carbonaceous Porous Network for High-Performance Organic Electrolyte Supercapacitors. *J. Mater. Chem. A* **2013**, *1* (24), 7000–7005.
- (43) Xu, P.; Gao, Q.; Ma, L.; Li, Z.; Zhang, H.; Xiao, H.; Liang, X.; Zhang, T.; Tian, X.; Liu, C. A High Surface Area N-Doped Holey Graphene Aerogel with Low Charge Transfer Resistance as High Performance Electrode of Non-Flammable Thermostable Supercapacitor. *Carbon* **2019**, *149*, 452–461.
- (44) Lu, W.; Liu, M.; Miao, L.; Zhu, D.; Wang, X.; Duan, H.; Wang, Z.; Li, L.; Xu, Z.; Gan, L.; et al. Nitrogen-Containing Ultramicroporous Carbon Nanospheres for High Performance Supercapacitor Electrodes. *Electrochim. Acta* **2016**, *205*, 132–141.
- (45) Xia, K.; Huang, Z.; Zheng, L.; Han, B.; Gao, Q.; Zhou, C.; Wang, H.; Wu, J. Facile and Controllable Synthesis of N/P Co-Doped Graphene for High-Performance Supercapacitors. *J. Power Sources* **2017**, *365*, 380–388.
- (46) Wan, L.; Shamsaei, E.; Easton, C. D.; Yu, D.; Liang, Y.; Chen, X.; Abbasi, Z.; Akbari, A.; Zhang, X.; Wang, H. ZIF-8 Derived Nitrogen-Doped Porous Carbon/Carbon Nanotube Composite for High-Performance Supercapacitor. *Carbon* **2017**, *121*, 330–336.
- (47) Jiang, J.; Chen, H.; Wang, Z.; Bao, L.; Qiang, Y.; Guan, S.; Chen, J. Nitrogen-Doped Hierarchical Porous Carbon Microsphere through KOH Activation for Supercapacitors. *J. Colloid Interface Sci.* **2015**, *452*, 54–61.
- (48) Ma, F.; Zhao, H.; Sun, L.; Li, Q.; Huo, L.; Xia, T.; Gao, S.; Pang, G.; Shi, Z.; Feng, S. A Facile Route for Nitrogen-Doped Hollow Graphitic Carbon Spheres with Superior Performance in Supercapacitors. *J. Mater. Chem.* **2012**, *22* (27), 13464–13468.
- (49) Yoo, J. J.; Balakrishnan, K.; Huang, J.; Meunier, V.; Sumpter, B. G.; Srivastava, A.; Conway, M.; Mohana Reddy, A. L.; Yu, J.; Vajtai, R.; et al. Ultrathin Planar Graphene Supercapacitors. *Nano Lett.* **2011**, *11* (4), 1423–1427.
- (50) Miller, J. R.; Outlaw, R. A.; Holloway, B. C. Graphene Double-Layer Capacitor with Ac Line-Filtering Performance. *Science* **2010**, *329*, 1637–1639.
- (51) Ma, X.; Hong, X.; He, L.; Xu, L.; Zhang, Y.; Zhu, Z.; Pan, X.; Zhu, J.; Mai, L. High Energy Density Micro-Supercapacitor Based on a Three-Dimensional Bicontinuous Porous Carbon with Interconnected Hierarchical Pores. *ACS Appl. Mater. Interfaces* **2019**, *11*, 948–956.
- (52) Liu, P.; Weng, X.; Liu, Z.; Zhang, Y.; Qiu, Q.; Wang, W.; Zhou, M.; Cai, W.; Ni, M.; Liu, M.; et al. High-Performance Quasi-Solid-State Supercapacitor Based on CuO Nanoparticles with Commercial-Level Mass Loading on Ceramic Material La_{1-x}Sr_xCoO_{3-δ} as Cathode. *ACS Appl. Energy Mater.* **2019**, *2*, 1480–1488.
- (53) Zhang, L.; Yang, X.; Zhang, F.; Long, G.; Zhang, T.; Leng, K.; Zhang, Y.; Huang, Y.; Ma, Y.; Zhang, M.; et al. Controlling the Effective Surface Area and Pore Size Distribution of Sp² Carbon Materials and Their Impact on the Capacitance Performance of These Materials. *J. Am. Chem. Soc.* **2013**, *135* (15), 5921–5929.
- (54) Gutiérrez, M. C.; Picó, F.; Rubio, F.; Manuel Amarilla, J.; Javier Palomares, F.; Ferrer, M. L.; Del Monte, F.; Rojo, J. M. PPO 15 -PEO 22 -PPO 15 Block Copolymer Assisted Synthesis of Monolithic Macro- and Microporous Carbon Aerogels Exhibiting High Conductivity and Remarkable Capacitance. *J. Mater. Chem.* **2009**, *19* (9), 1236–1240.
- (55) Zheng, X.; Zhang, K.; Yao, L.; Qiu, Y.; Wang, S. Hierarchically porous sheath-core graphene-based fiber-shaped supercapacitors with high energy density. *J. Mater. Chem. A* **2018**, *6* (3), 896–907.
- (56) Bi, Z.; Kong, Q.; Cao, Y.; Sun, G.; Su, F. Biomass-Derived Porous Carbon Materials with Different Dimensions for Supercapacitor Electrodes: A Review. *J. Mater. Chem. A* **2019**, *7*, 16028–16045.
- (57) Tian, W.; Zhang, H.; Sun, H.; Tadé, M. O.; Wang, S. Template-Free Synthesis of N-Doped Carbon with Pillared-Layered Pores as Bifunctional Materials for Supercapacitor and Environmental Applications. *Carbon* **2017**, *118*, 98–105.
- (58) Puthusseri, D.; Aravindan, V.; Madhavi, S.; Ogale, S. 3D Micro-Porous Conducting Carbon Beehive by Single Step Polymer Carbonization for High Performance Supercapacitors: The Magic of in Situ Porogen Formation. *Energy Environ. Sci.* **2014**, *7* (2), 728–735.
- (59) Pan, L.; Wang, Y.; Hu, H.; Li, X.; Liu, J.; Guan, L.; Tian, W.; Wang, X.; Li, Y.; Wu, M. 3D Self-Assembly Synthesis of Hierarchical Porous Carbon from Petroleum Asphalt for Supercapacitors. *Carbon* **2018**, *134*, 345–353.

(60) Liang, Q.; Ye, L.; Huang, Z.; Xu, Q.; Bai, Y.; Kang, F.; Yang, Q. A Honeycomb-like Porous Carbon Derived from Pomelo Peel for Use in High-Performance Supercapacitors. *Nanoscale* **2014**, *6* (22), 13831–13837.

(61) Wei, X.; Jiang, X.; Wei, J.; Gao, S. Functional Groups and Pore Size Distribution Do Matter to Hierarchically Porous Carbons as High-Rate-Performance Supercapacitors. *Chem. Mater.* **2016**, *28*, 445–458.